

# Superionic conduction in low-dimensional-networked anti-perovskites

Ziheng Lu<sup>a,b</sup>, Jiapeng Liu<sup>a</sup>, Francesco Ciucci<sup>a,c,\*</sup>

<sup>a</sup> Department of Mechanical and Aerospace Engineering, The Hong Kong University of Science and Technology, Clear Water Bay, Hong Kong, China

<sup>b</sup> Shenzhen Institute of Advanced Technology, Chinese Academy of Science, 1068 Xueyuan Avenue, Shenzhen University Town, Shenzhen, China

<sup>c</sup> Department of Chemical and Biomolecular Engineering, The Hong Kong University of Science and Technology, Clear Water Bay, Hong Kong, China

## ARTICLE INFO

### Keywords:

Superionic conductors  
Solid state batteries  
Lattice softening  
Density functional theory

## ABSTRACT

Fast cationic conduction is necessary for a number of solid-state technologies and is particularly critical for solid-state batteries as solid electrolytes are typically poor conductors. This article illustrates the concept of low-dimensional networked (low-DN) anti-perovskite via first-principles computations and shows that superionicity (i.e. the conductivity is above  $1 \text{ mS cm}^{-1}$  at room temperature) can be achieved by lowering the dimensionality of the connected octahedra of the anti-perovskite. In particular, we use the Li–O–Cl model system and study the diffusion of Li in 3DN-Li<sub>3</sub>OCl, 2DN-Li<sub>4</sub>OCl<sub>2</sub>, 1DN-Li<sub>5</sub>OCl<sub>3</sub>, and 0DN-Li<sub>6</sub>OCl<sub>4</sub>. We find that the lower the dimensionality, the lower the Li migration barriers and the higher the diffusion coefficients are. We attribute this improved ionic conduction to the decreased size of the bottlenecks and the softening of the rotation modes of the octahedra in the structure. To further explore the concept of low-DN anti-perovskites, we screen 256 model materials in the I–VI–VII group chemical space by computing the phase stability and bandgap of 3DN-X<sub>3</sub>BA, 2DN-X<sub>4</sub>BA<sub>2</sub>, 1DN-X<sub>5</sub>BA<sub>3</sub>, and 0DN-X<sub>6</sub>BA<sub>4</sub> (X = Li, Na, K, Rb; B = O, S, Se, Te; and A = F, Cl, Br, I). The calculations suggest that 20% of the structures might be synthesized and a number of them possess reasonable cationic migration barriers (<400 meV). This study puts forward a new principle for designing solid superionic conductors by lowering the dimensionality of the primitive structural units.

## 1. Introduction

Perovskites have found applications in fields as diverse as solar cells [1–6], catalysts [7–9], fuel cells [10–12], lithium batteries [13–16], and piezoelectrics [17–20], due to their broad array of functional properties. A prototypical cubic perovskite has an ABX<sub>3</sub> composition. In a perfect crystal, six X-site anions surround one B-site cation to form a connected octahedron, and the A-site cations fill the space between the networked octahedra. Since the BX<sub>6</sub> units are connected, many perovskites display fast anionic conduction if defects are present [11,13,16,21,22]. Recently, anti-perovskites have also been discovered to be excellent ionic conductors [23]. A prototypical material in this family has the composition of Li<sub>3</sub>OA (A = Cl and Br), and its structure is shown in Fig. 1 (a). Unlike perovskites, the octahedral vertices of the defect-free crystal are occupied by positively charged Li<sup>+</sup> and negatively charged O<sup>2-</sup> and are positioned at the center of the unit cell. Since the Li<sup>+</sup> on the vertices are shared by neighboring OLi<sub>6</sub> units, these octahedra form a 3D Li<sup>+</sup> network. The connectivity of the OLi<sub>6</sub> octahedra enables the hopping of Li ions and thus endows the material with an ionic conductivity as high as  $10^{-3} \text{ S cm}^{-1}$  at room temperature (RT) [23].

$\text{cm}^{-1}$  at room temperature (RT) [23].

Despite their good conductivity, the lithium conduction mechanism in these superionic conductors is still not fully understood and has attracted significant attention [24]. Zhao et al. have suggested that a large number of defects are present in the material due to the complex thermal history encountered by these materials during their synthesis [23]. Zhang et al. [25] and Deng et al. [26] computed, using first-principles methods, that the hopping barrier of Li-vacancy are between 0.3 and 0.4 eV. Emly and co-workers calculated the diffusion barrier of Li interstitials is instead 0.15 eV [27]. However, the formation energy of Li interstitials in Frenkel pairs (Li interstitials + Li vacancies) is high (>1.5 eV), suggesting a low concentration. Mouta et al. used classical force fields and discussed the possibility of O substitution on Cl as an alternative charge compensation mechanism for the formation of Li-interstitials, see Section 3 of supplementary information (SI) for the defect reaction [28,29]. These researchers suggested that such interstitials are easier to form compared with Li Frenkel pairs. Our group calculated disassociation energies between a number of charged defects, including Li interstitials and O-site substitutional defects. We found a

\* Corresponding author. Department of Mechanical and Aerospace Engineering, The Hong Kong University of Science and Technology, Clear Water Bay, Hong Kong, China.

E-mail address: [francesco.ciucci@ust.hk](mailto:francesco.ciucci@ust.hk) (F. Ciucci).

<https://doi.org/10.1016/j.ensm.2020.03.005>

Received 4 November 2019; Received in revised form 3 March 2020; Accepted 3 March 2020

Available online 6 March 2020

2405-8297/© 2020 Elsevier B.V. All rights reserved.

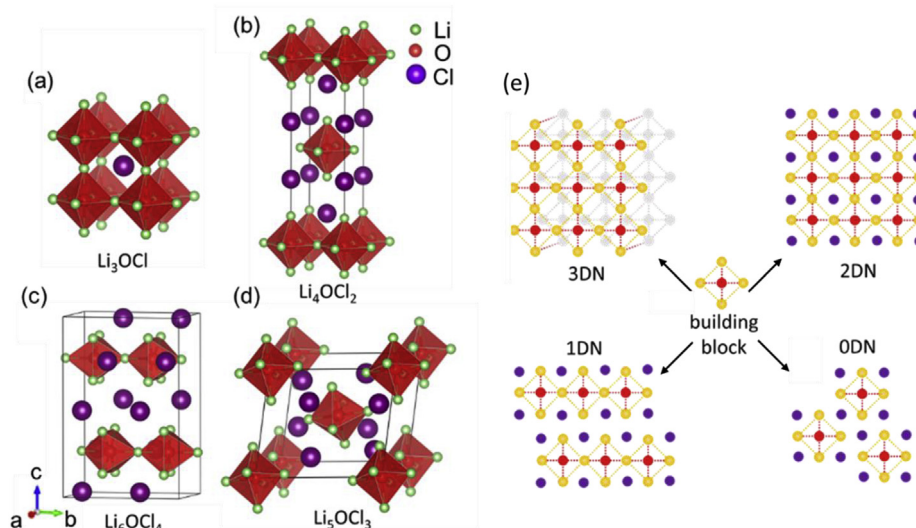


**Fig. 1.** Unit cells of (a) 3D- $\text{Li}_3\text{OCl}$ , (b) 2D- $\text{Li}_4\text{OCl}_2$ , (c) 1D- $\text{Li}_6\text{OCl}_4$ , and (d) 0D- $\text{Li}_5\text{OCl}_3$  anti-perovskites. (e) Illustration of the connectivity of low-DN anti-perovskites. The octahedral units are indicated as the building block, and the rest of the space is taken up by the A-site ions, which are signaled as purple dots. (For interpretation of the references to colour in this figure legend, the reader is referred to the Web version of this article.)

strong attractive interaction between these two, suggesting that the mobility of Li interstitials is limited by the countercharge defects generated [30]. Further molecular dynamics simulations suggest that LiCl Schottky pairs (Li vacancies + Cl vacancies) have activation energies close to those measured experimentally. Such results were later supported by Wu et al. who carried out density functional theory calculations and found Li vacancies interact less strongly with their countercharge defects compared with Li interstitials, leading to a faster cationic diffusion [31]. Recently, Stegmaier et al. calculated the formation energy of Li vacancies and interstitials as a function of the electrochemical potential of Li [32]. By computing charge carrier concentration, these authors found that, while Li vacancies contribute to the diffusivity in the bulk of the electrolyte and near the cathode, Li interstitials are favored at anodic potentials. Besides the bulk diffusion, the grain boundary conduction has also been investigated [33]. Dawson and co-workers used forcefield-based molecular dynamics simulations to simulate coherent grain boundaries in  $\text{Li}_3\text{OCl}$ . They found that such boundaries hinder the diffusion of Li. Recently, significant interest has also been drawn on the protonation of anti-perovskite solid electrolytes. It has been argued that protonation may enhance the phase stability of these materials, thereby facilitating their synthesis [34].

Apart from works aiming at elucidating the Li transport mechanism, significant efforts have also been devoted to designing materials with improved ionic conductivity [35,36]. Zhao et al. [23] and Deng et al. [26] proposed a halide anion mixing scheme to improve the ionic conductivity. These researchers found that by mixing Cl and Br to form a solid solution of  $\text{Li}_3\text{OCl}_{1-x}\text{Br}_x$  ( $0.235 \leq x \leq 0.395$ ), the Li cations diffuse faster than the end members,  $\text{Li}_3\text{OCl}$  and  $\text{Li}_3\text{OBr}$ . Sagotra et al. [37,38] and Mouta et al. [39] suggested that tensile biaxial mechanical stresses facilitate Li diffusion. Fang et al. predicted that introducing super halogen anions such as  $\text{BH}_4^-$  in the X site enlarge the diffusion channel and ultimately enhances the Li diffusivity [40]. Wang et al. suggested, via first-principles computations, that making double anti-perovskite may increase the Li conductivity [41]. Specifically, they computed that the double perovskite with a composition of  $\text{Li}_6\text{OSI}_2$  has a conductivity of  $5 \text{ mS cm}^{-1}$  at RT. Despite these significant advancements, the ionic conductivity of these anti-perovskites still needs improvements and novel design principle is desired.

Inspired by recent advances in low-dimensional perovskites in solar cells [42,43], we propose the concept of low-dimensional-networked (low-DN) anti-perovskite and investigate computationally the influence

of reducing the dimensionality of the connected octahedral units to increase the Li connectivity. Incidentally, we must point out that, while perovskites have been extensively investigated [44,45], anti-perovskites have been far less studied.

Low-DN anti-perovskites are derived from 3D anti-perovskites, see Fig. 1. Before discussing the structure of low-DN anti-perovskites, we must first remark that a 3D anti-perovskite has a  $\text{BX}_6$  octahedron as its basic structural unit, where a  $\text{B}^{2-}$  anion is surrounded by 6  $\text{X}^+$  cations. In the 3D  $\text{X}_3\text{BA}$  anti-perovskite, the  $\text{BX}_6$  octahedra form a cubic (sub)lattice. The  $\text{A}^-$  anions take up the remaining space in the structure and reside at the center of each cube. A typical 3D anti-perovskite  $\text{Li}_3\text{OCl}$  is shown in Fig. 1 (a). Low-DN anti-perovskites are obtained by lowering the dimensionality of the interconnected  $\text{BX}_6$  octahedra. For example, in a 2D anti-perovskite, the  $\text{BX}_6$  octahedra are connected along the (0 0 1) planes. The  $\text{BX}_6$  octahedra are separated perpendicularly to that direction by A-site anions. A typical 2D anti-perovskite  $\text{Li}_4\text{OCl}_2$  is shown in Fig. 1 (b). It is worth noting that such 2D structures are known as the Ruddlesden-Popper (RP) phases and have been used in the fields of oxygen catalysts and fuel cells [46]. Notable examples include  $\text{La}_{n+1}\text{Ni}_n\text{O}_{3n+1}$  and  $\text{Sr}_3\text{Fe}_2\text{O}_{6+\delta}$  [47,48]. Recently, Zhu et al. synthesized 2D  $\text{Li}_7\text{O}_2\text{Br}_3$  anti-perovskite [49]. Although these authors were not able to achieve a pure 2D phase, the mixture of the 2D phase and the 3D  $\text{Li}_3\text{OBr}$  displayed a significantly enhanced ionic conductivity ( $5 \times 10^{-5} \text{ S cm}^{-1}$ ) compared to  $\text{Li}_3\text{OBr}$  alone ( $10^{-6} \text{ S cm}^{-1}$ ). These results indicate that lowering the dimensionality of anti-perovskites improves the cationic conduction. The 1D and 0D anti-perovskites are compositionally similar to their 2D counterparts except that the dimensionality of the octahedral networks is reduced to 1 and 0, respectively. Representative 2D and 1D anti-perovskite structures in the Li–O–Cl chemical space are as shown in Fig. 1 (d) ( $\text{Li}_6\text{OCl}_4$ ) and Fig. 1 (e) ( $\text{Li}_5\text{OCl}_3$ ), respectively. While 1D and 0D anti-perovskite structures have yet to be reported, low-DN perovskites, such as  $\text{C}_4\text{N}_2\text{H}_{14}\text{PbBr}_4$  and  $\text{Cs}_4\text{PbBr}_6$ , have been investigated [50,51]. Due to their unique crystal structure, these materials exhibit desired electronic structures and showed exceptional photovoltaic performance.

## 2. Results and discussions

To study the impact of the anti-perovskite's dimensionality on ionic conduction, we used the Li–Cl–O system as a model composition. This choice is motivated by the fact that 3D- $\text{Li}_3\text{OCl}$  is the most studied Li-

rich anti-perovskite material [27,28,30,52,53]. The structure templates of the low-DN anti-perovskites are derived from a recent work by Xiao et al. [6] By comparing the compositions and the crystal structures of the anti-perovskites shown in Fig. 1, the lattice of low-DN structures can be understood as a modification of the 3DN ones by the addition of LiCl. We note that the extra  $\text{Cl}^-$  modifies the structure of 3DN- $\text{Li}_3\text{OCl}$  by separating the  $\text{OLi}_6$  units. A similar idea has been proposed in the area of glassy solid electrolytes, e.g.,  $\text{xLi}_2\text{S}(1-\text{x})\text{SiS}_2$ , where LiI was added to change the coordination of  $\text{Li}^+$  and the overall structure, thereby improving the ionic conductivity [54–56]. Since the Li conduction in crystals materials is a defect-mediated hopping process, we use the hopping barrier to first assess the ease of Li diffusion. The barrier is evaluated using the nudged elastic band (NEB) method; details are given in Section 1 of the SI. We first compute the defect formation energy to determine which type of defect mediates the Li hopping. As shown in Table S1, the results point to the fact that Li vacancies are the main charge carrier, in agreement with the recent theoretical works [41,57]. Therefore, as a descriptor of the Li diffusivity, we calculate the barrier of Li hopping as mediated only by vacancies. In low-DN Li-rich anti-perovskites, the Li paths can be categorized into two distinct types. The first type of path is an intrachain jump within the  $\text{OLi}_6$  octahedron along one of its 8 edges. The other path type is the one between separate  $\text{OLi}_6$  octahedra. The diffusion barrier in either type of path reduces as the

dimensionality of the anti-perovskite decreases. For the 3DN- $\text{Li}_3\text{OCl}$ , since  $\text{OLi}_6$  octahedra are all connected, as shown in Fig. 2 (a), only intrachain diffusion is possible with a computed migration barrier of 370 meV, a value consistent with previous publications [25,27,31]. In the 2DN (or RP) anti-perovskite phase, two distinct types of Li sites are present. One type of Li site is in the same plane as O, and the other is in the same plane as Cl. This leads to 2 different intrachain hopping paths. The barrier of Li hopping within the Li–O plane is  $\sim 380$  meV, a value close to that computed for the 3DN material. In contrast, the Li hopping barrier between the Li–O plane and Li–Cl planes is lower (310 meV). Since a lower barrier implies that the diffusion is more probable, the intrachain diffusion for the 2DN-perovskite is likely faster compared to that taking place in the 3DN material. In 2DN anti-perovskites, interchain paths also need to be analyzed. Not surprisingly, the interchain diffusion between two  $\text{OLi}_6$ -containing layers is about 800 meV. This value is so high that interchain hops are far less likely in 2DN anti-perovskites. The Li hops in the 1DN-perovskite display similar energetics as those encountered in the 2DN material. For the intrachain hopping, two types of paths are possible. One involves the Li moving along the 1D chain as indicated with the black arrow in Fig. 2 (c) (right panel). The barrier for this path is 211 meV. The other path has a much lower barrier, approximately 60 meV. However, we note that this path does not contribute to the conductivity because it is not percolative, see the inset of Fig. 2 (c) (right panel). Nonetheless, the highest intrachain diffusion barrier (211 meV) for the 1DN anti-perovskite is 100 meV lower than that computed for the 2DN and 3DN materials. The interchain hopping barrier (397 meV) of the 1DN anti-perovskite is also lower than the 2DN one. Since only the chains containing Li vacancies contribute to Li diffusion, such an interchain transport is the main contributor to the ionic conductivity. For the 0DN case, the intrachain diffusion degenerates into the circulation of Li cations around O. Such hopping events are expected to be frequent because of the low barrier (47 meV). However, they do not contribute to the overall diffusional path. Conversely, the hopping of Li between individual  $\text{OLi}_6$  octahedra is characterized by a low barrier of  $\sim 160$  meV as well. Such a value is significantly lower than that computed for the intrachain diffusion in 3DN anti-perovskites.

To support the results of the NEB calculations, we also performed *ab-initio* molecular dynamics simulations for the 4 anti-perovskite materials studied above. For each structure, we removed a single Li cation. As shown in Fig. 3, the diffusion of Li in all four types of low-DN anti-perovskites obeys an Arrhenius-type relation within the computed temperature range except for the 0DN- $\text{Li}_5\text{OCl}_3$ . We found that the material

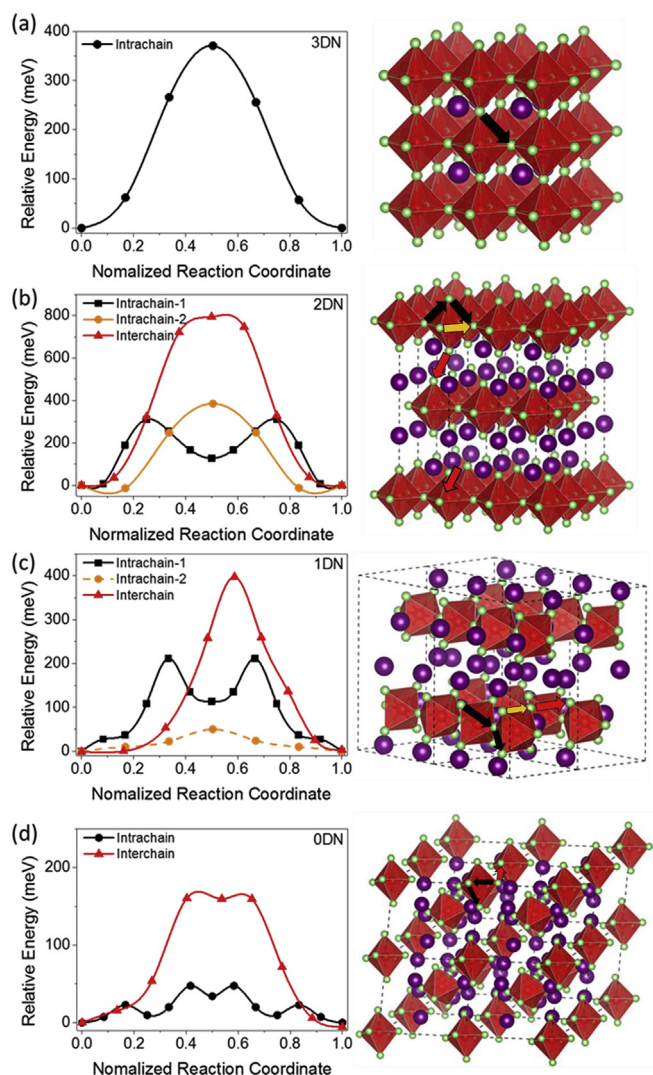


Fig. 2. Li diffusion barriers and corresponding diffusion paths in (a) 3DN- $\text{Li}_3\text{OCl}$ , (b) 2DN- $\text{Li}_4\text{OCl}_2$ , (c) 1DN- $\text{Li}_6\text{OCl}_4$ , and (d) 0DN- $\text{Li}_5\text{OCl}_3$  anti-perovskites.

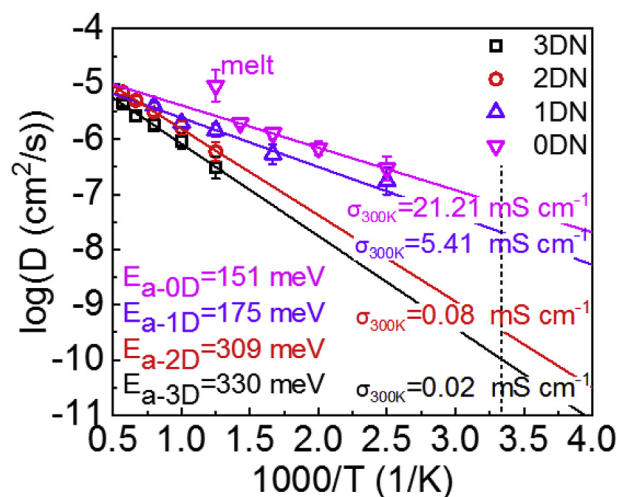


Fig. 3. Li diffusion coefficients obtained from *ab-initio* molecular dynamics simulations and extrapolated ionic conductivity at 300 K. To account for statistical errors, the confidence intervals reported in Table S2 of the SI are also shown.



melts at 800 K upon examining the trajectories. Considering that the MD simulations usually underestimate the melting temperature due to the absence of surfaces and the short simulation time, such a low melting temperature suggests phase instability. Therefore, whether this particular ODN phase can be synthesized will need to be assessed experimentally. We calculated the activation energies using Arrhenius relation and extrapolated the diffusion coefficient at 300 K. In 3DN-Li<sub>3</sub>OCl, the activation energy is 330 meV, a value very close to the one calculated using the NEB method and in good agreement with previous reports [26]. The Li diffusion coefficient was estimated to be  $\sim 10^{-10}$  cm<sup>2</sup> s<sup>-1</sup> at RT, in agreement with the AIMD simulations of Deng et al. as well as our classical MD simulations [26,30]. We also estimated the ionic conductivity  $\sigma$  using Einstein's relation [30]:  $\sigma = z|e|cD/kT$  where  $z$ ,  $c$ ,  $D$ ,  $k$ ,  $T$ , and  $|e|$  are the nominal charge Li<sup>+</sup>, the concentration of Li<sup>+</sup>, the diffusion coefficient of Li<sup>+</sup>, the Boltzmann constant, and temperature in Kelvin, respectively. The calculated conductivity of the Li<sub>3</sub>OCl is  $\sim 10^{-5}$  S cm<sup>-1</sup> which is lower than the experimental one reported by Zhao et al. [23]. However, considering the simulations here only show the intrinsic Li diffusivity without defect-defect interaction, it could be conjectured that real diffusivity is higher since the defect concentration in the system is greater than the one we simulated. The 2DN anti-perovskite has lower activation energy (309 meV) compared with its 3DN counterpart, in general agreement with the 311 meV found in the NEB calculations. The estimated 300 K conductivity is also slightly higher than that of 3DN-Li<sub>3</sub>OCl, i.e., 0.08 mS cm<sup>-1</sup>. For the 1DN and 0DN structures, there is a significant enhancement in Li diffusion with computed values of 5.4 mS cm<sup>-1</sup> and 21.2 mS cm<sup>-1</sup> at 300 K. Both materials achieve superionicity. The activation energies are also less than half of those of the 3DN Li<sub>3</sub>OCl, reaching 175 meV and 151 meV. These two values are among the best superionic conductors [58]. In summary, the enhancement in Li conductivity can be effectively achieved by reducing the dimensionality of the interconnected octahedra. It is important to note that the countercharge defects may significantly influence the diffusivity of Li [30].

Therefore, we also carried out AIMD simulations on the structures with LiCl defect pairs, see Fig. S1. The ionic conductivities computed for all structures with LiCl Schottky pair are 1/2 to 1/5 of those obtained without the Cl<sup>-</sup> counter charge defect, respectively. However, the conductivity order still hold, i.e., with the decrease in dimensionality, the ionic conductivity of LiCl-containing anti-perovskites increases. Additional details can be found in Section 4 of the SI.

It may be argued that the decreased diffusion barrier and enhanced conductivity of Li result from two factors: 1) the increase of bottleneck sizes for Li diffusion; and 2) the less rigid OLi<sub>6</sub> rotation, as the dimensionality is reduced. After careful examination of the structures, we found that the intrachain Li diffusion is restricted across the Cl–O–Cl bottleneck. Instead, the interchain Li diffusion is blocked by the Cl–Cl–Cl bottleneck. We computed the bottleneck sizes for all possible Li jumps and plotted the inter- and intra-chain diffusion bottlenecks in Fig. 4 (a). We found for both types of Li transport paths, the size of the bottleneck increases as the dimensionality of the anti-perovskite decreases. This geometrical trait supports the decreased Li diffusion barrier in low-DN structures. The actual values and analysis are outlined in Table S3 and in Section 5 of SI. The identified specific percolative paths are shown there as well. Also, phonon softening has been suggested to contribute to superionicity [59,60] as softer structural framework lowers the Li barriers [16,61,62]. The positive correlation between the softness octahedral rotation and ionic transport has also been reported in the field of oxygen transport by Li et al. for Ln<sub>2</sub>NiO<sub>4+δ</sub> (Ln = La, Pr, Nd), 2DN perovskites [63]. By noting that low-DN anti-perovskites have fewer geometrical constraints compared with their 3DN counterparts, one may conclude that the rotation of OLi<sub>6</sub> octahedra in low-DN anti-perovskites is easier, ultimately facilitating the Li diffusion. In order to evaluate the softness more quantitatively, we computed the phonon density of states of anti-perovskites. As shown in Fig. 4 (b) and 4 (c), the phonon band center, especially the Li-projected one, moves towards lower energies as the structural dimensionality decreases. In order to identify the particular

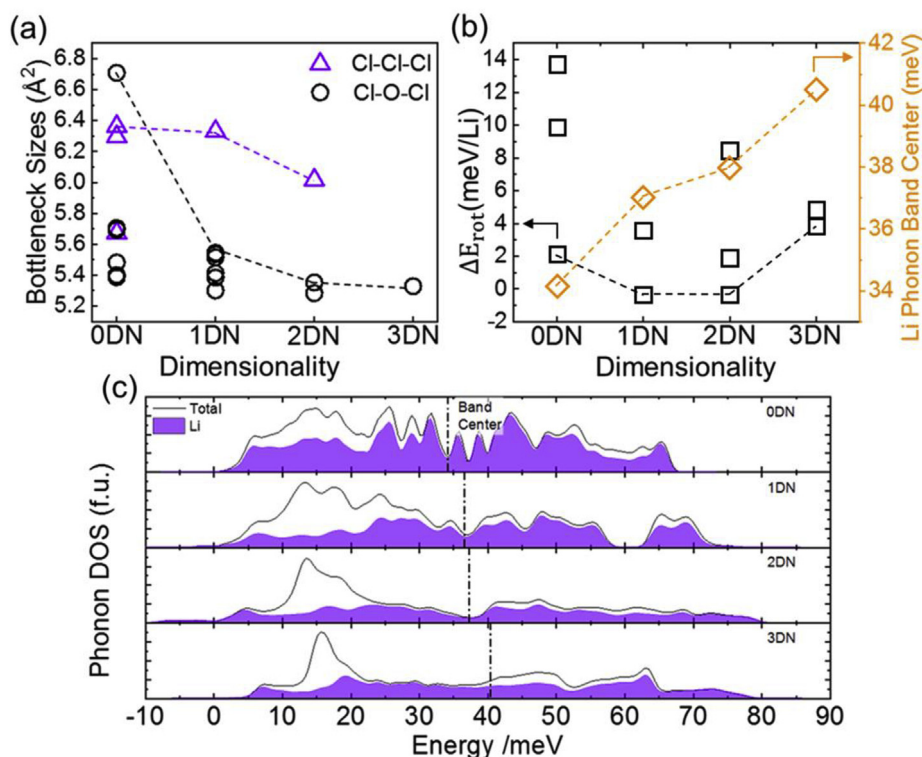


**Fig. 4.** (a) Sizes of the Li bottlenecks. Cl–O–Cl and Cl–Cl–Cl bottlenecks correspond to the intra- and inter-chain Li diffusion, respectively. (b) The rotation energy differences ( $\Delta E_{\text{rot}}$ ) between the structures with fixed OLi<sub>6</sub> octahedra and the structures with the OLi<sub>6</sub> octahedra rotated by 8° are plotted concurrently with the phonon band center. The dashed lines are shown to improve visual clarity. (c) Phonon density of states. The computation methods are included in Section 1 of SI.

soft phonon modes that facilitate Li diffusion, we calculated the energy needed to excite specific modes of  $\text{OLi}_6$  rotation in the Li–Cl–O anti-perovskites. The results are shown in Fig. 4 (b) with the specific rotation modes shown in Section 6 of the SI. 2DN, 1DN and 0DN anti-perovskites all have at least one rotation mode that is significantly softer than that of the 3DN material, indicating such rotation may be responsible for the fast Li diffusion.

The remaining question is whether low-DN anti-perovskites can be synthesized. To evaluate the phase stability, we computed the energy above hull (decomposition energy to form stable products) of 3DN- $\text{Li}_3\text{OCl}$ , 2DN- $\text{Li}_4\text{OCl}_2$ , 1DN- $\text{Li}_5\text{OCl}_3$ , and 0DN- $\text{Li}_6\text{OCl}_4$  by constructing phase diagrams based on GGA-PBE level density functional theory (DFT) calculations. A summary of the results is given in Table 1. All of the computed anti-perovskite phases are thermodynamically unstable at 0 K and decompose into LiCl and  $\text{Li}_2\text{O}$ . However, the decomposition energies for all structures except the 0DN- $\text{Li}_6\text{OCl}_4$  are relatively small ( $<30 \text{ meV atom}^{-1}$ ), indicating that entropic stabilization is possible. This result is in agreement with previous theoretical calculations, which suggest that  $\text{Li}_3\text{OCl}$  can be stabilized at  $\sim 500 \text{ K}$  [41,53]. Also, many superionic conductors are metastable (unstable at 0 K but with little energy above the hull and therefore likely stabilizable by entropy at finite temperature), but they are still synthesizable. Perhaps, the best-known example of a metastable superionic conductor is  $\text{Li}_{10}\text{GeP}_2\text{S}_{12}$ , which has an energy above hull of  $\sim 25 \text{ meV atom}^{-1}$  [64]. The meta-stability of  $\text{Li}_{10}\text{GeP}_2\text{S}_{12}$  cannot directly lead to the conclusion that all metastable low-DN anti-perovskites are synthesizable. However, we must note that in spite of their large energy above, the synthesis of 3DN anti-perovskites has been reported in particular [65]. In particular, the decomposition energy of the 2DN- $\text{Li}_4\text{OCl}_2$  (RP phase) is smaller than  $7 \text{ meV atom}^{-1}$ , a value close to the accuracy of GGA-PBE DFT calculations [66–68].

Apart from the ionic conductivity and phase stability, solid electrolytes also need to have a negligible electron conductivity and a wide electrochemical window. The bandgap is a widely used proxy for these two properties [64,69,70]. For all the 4 calculated materials, the band gaps are greater than 4.3 eV, indicating that these materials are good electron insulators and the intrinsic electrochemical window may be wide. The real electrochemical performance depends on the choice of electrode materials, and the related kinetics should thus be determined experimentally [71].

To extend the range of possible structures in the low-DN anti-perovskite family, we also calculated the formation energies of 256 materials chosen in the I–VI–VII group. The same structure templates as in the Li–O–Cl space were used, and specifically, 3DN- $\text{X}_3\text{BA}$ , 2DN- $\text{X}_4\text{BA}_2$ , 1DN- $\text{X}_5\text{BA}_3$ , and 0DN- $\text{X}_6\text{BA}_4$  ( $\text{X} = \text{Li, Na, K, Rb}$ ;  $\text{B} = \text{O, S, Se, Te}$ ; and  $\text{A} = \text{F, Cl, Br, I}$ ) were computed. The calculated energy above the hull is shown in Fig. 5 (a) with detailed entries listed in Table S4 in SI. 51 out of the 256 phases have a decomposition energy lower than  $75 \text{ meV/atom}$ , a threshold we set for synthesizability. We also gathered the statistics on the phase stability with respect to different factors including the dimensionality, the types of cations, the types of B-site anions, and the types of the A-site anions. As shown in Fig. 5 (b), the 3DN and 2DN

structures show dispersed distributions in decomposition energy, while the results for 1DN and 0DN materials display a narrower distribution. This may be because in our computations the low-DN structures have looser symmetry constraints. In fact, for the 3DN and 2DN anti-perovskites unit cells (instead of supercells) were used. For example, the 3DN anti-perovskites are assumed to be cubic. Such an assumption may lead to low phase stability, especially when the sizes of cations and anions do not match. The cation type appears to be less relevant to the stability of the structures. As shown in Fig. 5 (c), the distribution is similar among Li-, Na-, K-, and Rb-compounds, which all show a narrow peak around  $200 \text{ meV atom}^{-1}$  and a long tail. Unlike cations, anions have a significant impact on stability. Among the B-site anions (O, S, Se, and Te at the center of the octahedra), the ones with lower period number tend to result in more stable phases. We note that these results are in agreement with the findings by Ong et al. where the anions in Li-Ge-P-X ( $\text{X} = \text{O, S, Se, and Te}$ ) [72] series of materials have a profound influence on the phase stability of these LGPX compounds. Such a stabilization by lower-period-number B-site anions is perhaps occurring because the anions with lower period numbers are more electronegative and the bonds they form with X cations (Li, Na, K, and Rb at the vertices of the octahedron) have stronger ionic characters. Since the more ionic the bonds the lower is its directionality, the 8-fold coordination is likely to be energetically more favorable. For the A-site anions (F, Cl, Br, and I), the trend is the opposite to the one just described. The lower period number the lower the phase stability is. This is because anions with larger ionic sizes can better fill the lattice and contribute to the structural stability. In fact, we calculated the Goldschmidt tolerance factor which is a descriptor for the stability of cubic perovskite [73]. For all the materials we considered, the factors are  $<1$ , meaning the A-site ions are undersized and the layered structure is favored. The computation details are enclosed in Section 7 of SI. To further explore the possible use of the low-DN anti-perovskites, we performed AIMD simulations on the most synthesizable materials (with energy above hull  $< 20 \text{ meV}$ ) to assess their ionic conductivity. The ionic conductivity and the activation energies are shown in Table 2. Among the computed materials, two lithium-based anti-perovskites, i.e.,  $\text{Li}_5\text{OCl}_3$  and  $\text{Li}_6\text{OBr}_4$ , are predicted to be superionic conductors with a Li conductivity above  $10^{-3} \text{ S cm}^{-1}$ . Both of these two materials are 1DN. Such a result is in agreement with the previous discussions: 1DN structures give rise to high ionic conductivity but do not sacrifice the stability. Some Na conductors are also explored, such as 3DN- $\text{Na}_3\text{OBr}$  and 2DN- $\text{Na}_4\text{OBr}_2$  [74–76]. The latter materials show a Na conductivity close to  $10^{-4} \text{ S cm}^{-1}$ . Considering these materials may be synthesized and are computed to have high ionic conductivity, they hold considerable promise as solid electrolytes for Li and Na based solid-state batteries.

### 3. Conclusions

In this article, we propose the concept of low-DN anti-perovskite. We study the cation diffusion in anti-perovskites using Li–Cl–O as a model and find that reducing the dimensionality of the octahedral networks effectively lowers the Li diffusion barrier and facilitates its Li transport. Such improvement on Li diffusion is due to the enlarged bottleneck sizes for Li hopping as well as the softening of lattice. In particular, the 2DN- $\text{Li}_4\text{OCl}_2$ , 1DN- $\text{Li}_5\text{OCl}_3$ , and 0DN- $\text{Li}_6\text{OCl}_4$  are promising synthesizable superionic conductors. Further, the reduction in dimensionality also does not change the electron insulating nature of these materials, making them good candidates for solid electrolytes in solid-state batteries. To further extend the possible structures in the low-DN anti-perovskite family, we also screened 256 structures and found many other materials that could be potentially synthesized. These materials may offer new opportunities in solid-state batteries as well as other applications which are yet to be discovered. This study extends the family of anti-perovskites and provides a novel angle to the design of superionic conductors for solid-electrolytes as well as other applications.

**Table 1**

Energy above the hull and GGA band gaps of  $\text{Li}_3\text{OCl}$ ,  $\text{Li}_4\text{OCl}_2$ ,  $\text{Li}_5\text{OCl}_3$ , and  $\text{Li}_6\text{OCl}_4$ .

Phase	Energy above hull/ $\text{meV atom}^{-1}$	Band gap/ eV	Decomposition product
3DN- $\text{Li}_3\text{OCl}$	22	4.7	$\text{LiCl} + \text{Li}_2\text{O}$
2DN- $\text{Li}_4\text{OCl}_2$	7	4.4	
1DN- $\text{Li}_5\text{OCl}_3$	20	4.3	$\text{Li}_2\text{O}$
0DN- $\text{Li}_6\text{OCl}_4$	41	4.7	

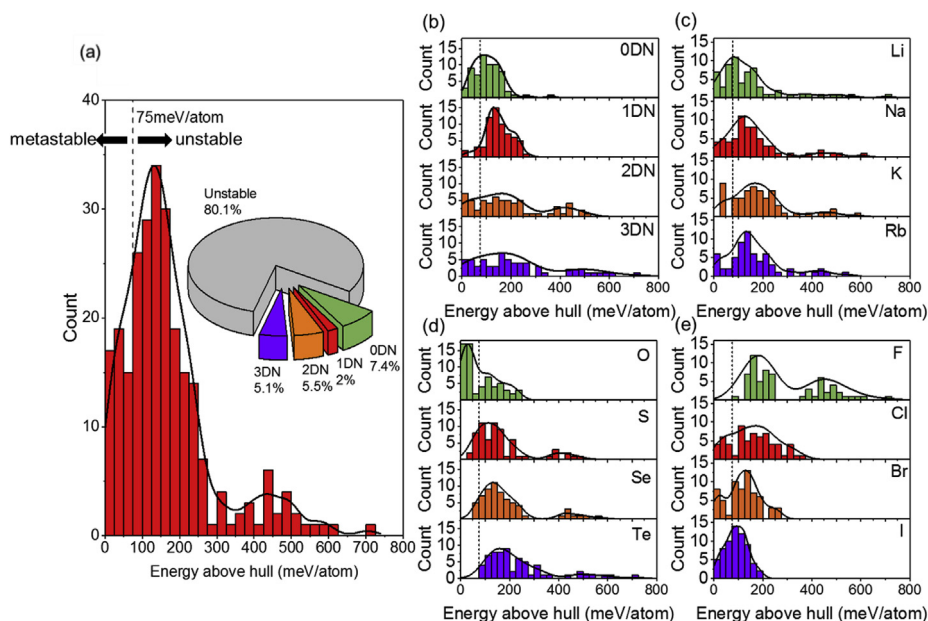


**Fig. 5.** Phase stability of anti-perovskites. Histogram of energy above hull of (a) all 256 model structures and structure classified by (b) 3DN, 2DN, 1DN and ODN; (c) A site element: F, Cl, Br, I; (d) B site element: O, S, Se, Te; and (e) X site element: Li, Na, K, Rb.

**Table 2**

Cation diffusion activation energies and the ionic conductivity of the most synthesizable phases (energy above hull <20 meV) predicted by AIMD simulations.

Phase	Energy above hull/eV atom <sup>-1</sup>	Cation	Conductivity at RT/S cm <sup>-1</sup>	Activation Energy/meV
3DN-Na <sub>3</sub> OBr	0	Na	$1.3 \times 10^{-5}$	392
3DN-Na <sub>3</sub> OI	0	Na	$2.1 \times 10^{-7}$	453
2DN-Na <sub>4</sub> OBr <sub>2</sub>	0	Na	$8.1 \times 10^{-5}$	342
2DN-Na <sub>4</sub> OI <sub>2</sub>	0	Li	$3.1 \times 10^{-6}$	410
2DN-Li <sub>4</sub> OBr <sub>2</sub>	0	Li	$1.1 \times 10^{-4}$	325
2DN-Li <sub>4</sub> OCl <sub>2</sub>	0.006	Li	$4.0 \times 10^{-5}$	331
3DN-Li <sub>3</sub> OBr	0.013	Li	$6.1 \times 10^{-6}$	410
2DN-Rb <sub>4</sub> OI <sub>2</sub>	0.017	Rb	$<10^{-8}$	920 <sup>a</sup>
2DN-Li <sub>4</sub> OI <sub>2</sub>	0.017	Li	$5.2 \times 10^{-5}$	360
2DN-Rb <sub>4</sub> OBr <sub>2</sub>	0.018	Rb	$<10^{-8}$	856 <sup>a</sup>
3DN-Rb <sub>3</sub> OBr	0.019	Li	$<10^{-8}$	870 <sup>a</sup>
1DN-Li <sub>6</sub> OBr <sub>4</sub>	0.019	Li	$1.1 \times 10^{-3}$	172
1DN-Li <sub>6</sub> OCl <sub>4</sub>	0.02	Li	$7.4 \times 10^{-3}$	152

<sup>a</sup> We were not able to sample enough hopping events in Rb-based materials even at elevated simulation temperatures over 1500 K due to the slow cationic diffusion. Therefore we estimated their activation energies based on NEB calculations.

## Credit

Ziheng Lu: Conceptualization, Investigation, Writing - Original draft preparation, Writing - Review & Editing. Jiapeng Liu: Investigation, Writing - Original draft preparation. Francesco Ciucci: Conceptualization, Supervision, Investigation, Writing - Review & Editing, Funding acquisition.

## Declaration of competing interest

The authors declare that they have no known competing financial interests or personal relationships that could have appeared to influence the work reported in this paper.

## Acknowledgments

The authors gratefully acknowledges the Research Grants Council of Hong Kong for support through the projects 16207615, 16227016, and 16204517, the Guangzhou Science and Technology Program (No. 2016201604030020), and the Science and Technology Program of Nansha District (No. 2015CX009).

## Appendix A. Supplementary data

Supplementary data to this article can be found online at <https://doi.org/10.1016/j.ensm.2020.03.005>.

## References

- [1] M. Grätzel, *Nat. Mater.* 13 (2014) 838.
- [2] N.J. Jeon, J.H. Noh, Y.C. Kim, W.S. Yang, S. Ryu, S.I. Seok, *Nat. Mater.* 13 (2014) 897.
- [3] M.A. Green, A. Ho-Baillie, H.J. Snaith, *Nat. Photon.* 8 (2014) 2134, *nphoton*. 2014.
- [4] Y. Li, B. Xu, H. Xu, H. Duan, X. Lü, S. Xin, W. Zhou, L. Xue, G. Fu, A. Manthiram, *Angew. Chem. Int. Ed.* 56 (2017) 753–756.
- [5] S. Albrecht, B. Rech, *Nat. Energy* 2 (2017) 16196.
- [6] Z. Xiao, W. Meng, J. Wang, D.B. Mitzi, Y. Yan, *Mater. Horiz.* 4 (2017) 206–216.
- [7] W. Wang, M.O. Tadé, Z. Shao, *Chem. Soc. Rev.* 44 (2015) 5371–5408.
- [8] D. Chen, C. Chen, Z.M. Baiyee, Z. Shao, F. Ciucci, *Chem. Rev.* 115 (2015) 9869–9921.
- [9] A. Grimaud, K.J. May, C.E. Carlton, Y.-L. Lee, M. Risch, W.T. Hong, J. Zhou, Y. Shao-Horn, *Nat. Commun.* 4 (2013) 2439.
- [10] Y. Zhou, X. Guan, H. Zhou, K. Ramadoss, S. Adam, H. Liu, S. Lee, J. Shi, M. Tsuchiya, D.D. Fong, *Nature* 534 (2016) 231.
- [11] Z. Shao, S.M. Haile, A high-performance cathode for the next generation of solid-oxide fuel cells, in: *Materials for Sustainable Energy: A Collection of Peer-Reviewed Research and Review Articles from Nature Publishing Group, World Scientific*, 2011, pp. 255–258.

- [12] J. Suntivich, H.A. Gasteiger, N. Yabuuchi, H. Nakanishi, J.B. Goodenough, Y. Shao-Horn, *Nat. Chem.* 3 (2011) 546.
- [13] Y. Inaguma, C. Lique, M. Itoh, T. Nakamura, T. Uchida, H. Ikuta, M. Wakihara, *Solid State Commun.* 86 (1993) 689–693.
- [14] H. Kawai, J. Kuwano, *J. Electrochem. Soc.* 141 (1994) L78–L79.
- [15] P. Knauth, *Solid State Ionics* 180 (2009) 911–916.
- [16] J.C. Bachman, S. Muy, A. Grimaud, H.-H. Chang, N. Pour, S.F. Lux, O. Paschos, F. Maglia, S. Lupart, P. Lamp, *Chem. Rev.* 116 (2015) 140–162.
- [17] S. Zhang, R. Xia, T.R. Shrout, G. Zang, J. Wang, *J. Appl. Phys.* 100 (2006) 104108.
- [18] T.R. Shrout, S.J. Zhang, *J. Electroceram.* 19 (2007) 113–126.
- [19] J. Kuwata, K. Uchino, S. Nomura, *Jpn. J. Appl. Phys.* 21 (1982) 1298.
- [20] K.-I. Park, S. Xu, Y. Liu, G.-T. Hwang, S.-J.L. Kang, Z.L. Wang, K.J. Lee, *Nano Lett.* 10 (2010) 4939–4943.
- [21] G. Kim, S. Wang, A. Jacobson, L. Reimus, P. Brodersen, C. Mims, *J. Mater. Chem.* 17 (2007) 2500–2505.
- [22] F. Dong, M. Ni, Y. Chen, D. Chen, M.O. Tadé, Z. Shao, *J. Mater. Chem.* 2 (2014) 20520–20529.
- [23] Y. Zhao, L.L. Daemen, *J. Am. Chem. Soc.* 134 (2012) 15042–15047.
- [24] H.H. Heenen, J. Voss, C. Scheurer, K. Reuter, A.C. Luntz, *J. Phys. Chem. Lett.* 10 (2019) 2264–2269.
- [25] Y. Zhang, Y. Zhao, C. Chen, *Phys. Rev. B* 87 (2013) 134303.
- [26] Z. Deng, B. Radhakrishnan, S.P. Ong, *Chem. Mater.* 27 (2015) 3749–3755.
- [27] A. Emly, E. Kioupakis, A. Van der Ven, *Chem. Mater.* 25 (2013) 4663–4670.
- [28] R. Mouta, M.A.B. Melo, E.M. Diniz, C.W.A. Paschoal, *Chem. Mater.* 26 (2014) 7137–7144.
- [29] R. Mouta, E. Diniz, C. Paschoal, *J. Mater. Chem.* 4 (2016) 1586–1590.
- [30] Z. Lu, C. Chen, Z.M. Baiyee, X. Chen, C. Niu, F. Ciucci, *Phys. Chem. Chem. Phys.* 17 (2015) 32547–32555.
- [31] M. Wu, B. Xu, X. Lei, K. Huang, C. Ouyang, *J. Mater. Chem.* 6 (2018) 1150–1160.
- [32] S. Stegmaier, J. Voss, K. Reuter, A.C. Luntz, *Chem. Mater.* 29 (2017) 4330–4340.
- [33] J.A. Dawson, P. Canepa, T. Famprikis, C. Masquelier, M.S. Islam, *J. Am. Chem. Soc.* 140 (2017) 362–368.
- [34] I. Hanghofer, G.N.J. Redhammer, S. Rohde, I. Hanzu, A. Senyshyn, H.M.R. Wilkening, D. Rettenwander, *Chem. Mater.* 30 (2018) 8134–8144.
- [35] H. Xu, M. Xuan, W. Xiao, Y. Shen, Z. Li, Z. Wang, J. Hu, G. Shao, *ACS Appl. Energy Mater.* 2 (2019) 6288–6294.
- [36] S. Shi, J. Gao, Y. Liu, Y. Zhao, Q. Wu, W. Ju, C. Ouyang, *R. Xian, Chin. Phys. B* 25 (2016), 018212.
- [37] A.K. Sagotra, C. Cazorla, *ACS Appl. Mater. Interfaces* 9 (2017) 38773–38783.
- [38] A.K. Sagotra, D. Errandonea, C. Cazorla, *Nat. Commun.* 8 (2017) 963.
- [39] R. Mouta, C. Paschoal, *arXiv preprint arXiv:1603.04830*, (2016).
- [40] H. Fang, P. Jena, *Proc. Natl. Acad. Sci. Unit. States Am.* (2017) 201704086.
- [41] Z. Wang, H. Xu, M. Xuan, G. Shao, *J. Mater. Chem.* 6 (2018) 73–83.
- [42] L. Etgar, *Energy Environ. Sci.* 11 (2018) 234–242.
- [43] M.I. Saidaminov, O.F. Mohammed, O.M. Bakr, *ACS Energy Lett.* 2 (2017) 889–896.
- [44] C. Zhou, H. Lin, Q. He, L. Xu, M. Worku, M. Chaaban, S. Lee, X. Shi, M.-H. Du, B. Ma, *Mater. Sci. Eng. R Rep.* 137 (2019) 38–65.
- [45] K. Hong, Q. Van Le, S.Y. Kim, H.W. Jang, *J. Mater. Chem. C* 6 (2018) 2189–2209.
- [46] G. Amow, S. Skinner, *J. Solid State Electrochem.* 10 (2006) 538–546.
- [47] G. Amow, I. Davidson, S. Skinner, *Solid State Ionics* 177 (2006) 1205–1210.
- [48] F. Prado, L. Moggi, G. Cuello, A. Caneiro, *Solid State Ionics* 178 (2007) 77–82.
- [49] J. Zhu, S. Li, Y. Zhang, J.W. Howard, X. Lü, Y. Li, Y. Wang, R.S. Kumar, L. Wang, Y. Zhao, *Appl. Phys. Lett.* 109 (2016) 101904.
- [50] Z. Yuan, C. Zhou, Y. Tian, Y. Shu, J. Messier, J.C. Wang, L.J. Van De Burgt, K. Kountouriotis, Y. Xin, E. Holt, *Nat. Commun.* 8 (2017) 14051.
- [51] M.I. Saidaminov, J. Almutlaq, S. Sarmah, I. Dursun, A.A. Zhumekenov, R. Begum, J. Pan, N. Cho, O.F. Mohammed, O.M. Bakr, *ACS Energy Lett.* 1 (2016) 840–845.
- [52] X. Lü, G. Wu, J.W. Howard, A. Chen, Y. Zhao, L.L. Daemen, Q. Jia, *Chem. Commun.* 50 (2014) 11520–11522.
- [53] M.-H. Chen, A. Emly, A. Van der Ven, *Phys. Rev. B* 91 (2015) 214306.
- [54] A. Pradel, M. Ribes, *Solid State Ionics* 18 (1986) 351–355.
- [55] C.-H. Lee, K. Joo, J. Kim, S. Woo, H.-J. Sohn, T. Kang, Y. Park, J. Oh, *Solid State Ionics* 149 (2002) 59–65.
- [56] K. Padmasree, D. Kanchan, A. Kulkarni, *Solid State Ionics* 177 (2006) 475–482.
- [57] Y. Yu, Z. Wang, G. Shao, *J. Mater. Chem.* 6 (2018) 19843–19852.
- [58] Z. Zhang, Y. Shao, B. Lotsch, Y.-S. Hu, H. Li, J. Janek, L.F. Nazar, C.-W. Nan, J. Maier, M. Armand, *Energy Environ. Sci.* 11 (2018) 1945–1976.
- [59] K. Wakamura, *Phys. Rev. B* 56 (1997) 11593.
- [60] P. Goel, N. Choudhury, S. Chaplot, *Phys. Rev. B* 70 (2004) 174307.
- [61] M.A. Kraft, S.P. Culver, M. Calderon, F. Böcher, T. Krauskopf, A. Senyshyn, C. Dietrich, A. Zevalkink, J.R. Janek, W.G. Zeier, *J. Am. Chem. Soc.* 139 (2017) 10909–10918.
- [62] S. Muy, J.C. Bachman, L. Giordano, H.-H. Chang, D.L. Abernathy, D. Bansal, O. Delaire, S. Hori, R. Kanno, F. Maglia, *Energy Environ. Sci.* 11 (2018) 850–859.
- [63] X. Li, N.A. Benedek, *Chem. Mater.* 27 (2015) 2647–2652.
- [64] Y. Mo, S.P. Ong, G. Ceder, *Chem. Mater.* 24 (2011) 15–17.
- [65] J.A. Dawson, T.S. Attari, H. Chen, S.P. Emge, K.E. Johnston, M.S. Islam, *Energy Environ. Sci.* 11 (2018) 2993–3002.
- [66] S. Kirklin, J.E. Saal, B. Meredig, A. Thompson, J.W. Doak, M. Aykol, S. Rühl, C. Wolverton, *npj Comput. Mater.* 1 (2015) 15010.
- [67] A. Urban, D.-H. Seo, G. Ceder, *npj Comput. Mater.* 2 (2016) 16002.
- [68] Y. Zhang, D.A. Kitchaev, J. Yang, T. Chen, S.T. Dacek, R.A. Sarmiento-Pérez, M.A. Marques, H. Peng, G. Ceder, J.P. Perdew, *npj Comput. Mater.* 4 (2018) 9.
- [69] Z. Lu, F. Ciucci, *Chem. Mater.* 29 (2017) 9308–9319.
- [70] Y. Zhu, X. He, Y. Mo, *ACS Appl. Mater. Interfaces* 7 (2015) 23685–23693.
- [71] F. Han, Y. Zhu, X. He, Y. Mo, C. Wang, *Adv. Energy Mater.* 6 (2016) 1501590.
- [72] S.P. Ong, Y. Mo, W.D. Richards, L. Miara, H.S. Lee, G. Ceder, *Energy Environ. Sci.* 6 (2013) 148–156.
- [73] V.M. Goldschmidt, *Naturwissenschaften* 14 (1926) 477–485.
- [74] H. Sabrowsky, K. Paszkowski, D. Reddig, P. Vogt, *Z. Naturforsch. B Chem. Sci.* 43 (1988) 238–239.
- [75] K. Hippler, S. Sitta, P. Vogt, H. Sabrowsky, *Z. Naturforsch. B Chem. Sci.* 45 (1990) 105–106.
- [76] J. Zhu, Y. Wang, S. Li, J.W. Howard, J.R. Neufeld, Y. Ren, H. Wang, C. Liang, W. Yang, R. Zou, *Inorg. Chem.* 55 (2016) 5993–5998.